Received: 31 March 2021 | Revised: 22 September 2021 | Accepted: 12 October 2021

DOI: 10.1002/esp.5286

RESEARCH ARTICLE

ESPL WILEY

Connectivity and directionality in estuarine channel networks

Matthew Hiatt[1,2,3] | Elisabeth A. Addink[1] | Maarten G. Kleinhans[1]

[1]Department of Physical Geography, Faculty of Geosciences, Utrecht University, Utrecht, The Netherlands

[2]Department of Oceanography and Coastal Sciences, College of the Coast and Environment, Louisiana State University, Baton Rouge, Louisiana, USA

[3]Coastal Studies Institute, Louisiana State University, Baton Rouge, Louisiana, USA

Correspondence
Matthew Hiatt, Department of Oceanography and Coastal Sciences, College of the Coast and Environment, Louisiana State University, Baton Rouge, Louisiana, USA.
Email: mhiatt1@lsu.edu

Summary

Estuaries host channel networks that can range from meandering single-thread channels to complex channel networks comprising looping, branching, and offshoot structures through which water, sediment, and nutrients are transported in both the flood and ebb directions. In this article, we use graph theory to quantify the structural and dynamical connectivity of multidirectional estuarine channel networks using network analysis techniques rooted in graph theory that have proven useful for quantifying connectivity in river deltas. Networks from several estuaries around the world are extracted from satellite imagery and compared to a set of schematized networks that represent the end-member of the channel network structure and dynamics found in estuaries. Higher levels of structural connectivity are found for larger networks, which points to increased predilection for looping structures in networks with large numbers of channels. The real-world network structures contain signatures of both mutually evasive flood and ebb channels that typify alluvial estuaries, but also contain branching structures as either bifurcating delta-like structures or converging tidal patterns. The level of dynamical connectivity is modulated by flow direction through the network, with flood direction fluxes more broadly distributed throughout the network and fluxes in the ebb direction tending to be more localized. Analysis of dynamical connectivity also reveals a tidal asymmetry indicative of fluxes in flood–ebb dominant channels in estuaries. This study provides implications for understanding the self-organization of estuarine channel networks on which fluxes are partitioned through estuaries in the flood and ebb directions, and establishes a benchmark for analyzing multidirectional channel networks using graph theory.

KEYWORDS
connectivity, estuary, graph theory, network analysis, tidal asymmetry

1 | INTRODUCTION

Estuaries are semi-enclosed coastal water bodies that are located where river and sea waters meet. Estuaries often host networks of channels and bars that are shaped by the interplay of fluvial and marine processes (Brown & Davies, 2010; de Haas et al., 2018; Jeuken & Wang, 2010; Leuven et al., 2016; Robinson, 1960; Van der Wegen & Roelvink, 2012; van Veen, 1950), forming environments that are among the most productive in the world, provide a range of ecosystem services, and support economic activities (Kennish, 2002; Boerema & Meire, 2017). Channel networks in estuaries range significantly in complexity, from single-thread straight channels to multi-channel systems that bifurcate and recombine (Figure 1). Analyzing estuarine channel connectivity may provide insight into system processes, as has been done for tributary networks (Rodriguez-Iturbe & Rinaldo, 1997; Wohl et al., 2017), tidal networks (Fagherazzi et al., 1999; Rinaldo et al., 1999a, 1999b), deltas (Passalacqua, 2017; Tejedor et al., 2015a, 2015b, 2016), and braided rivers (Marra et al., 2014), but there exists no formal analysis of connectivity in estuaries.

Patterns of hydrological connectivity—the transfer of matter, energy, or organisms among various landscape elements via water-mediated transport (Bracken et al., 2013; Pringle, 2003; Tetzlaff et al., 2007)—provide information about the structure and function of

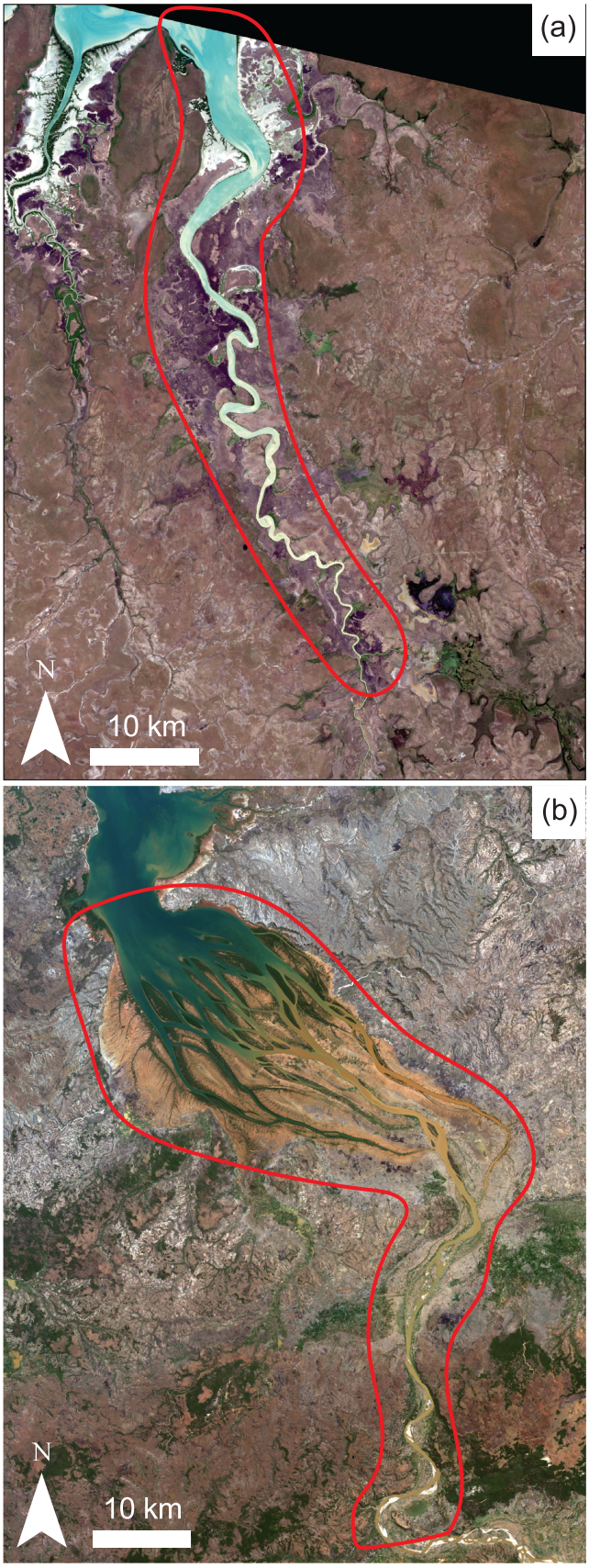

FIGURE 1 Examples of a single-thread channel network and a multi-channel network. (a) South Alligator River Estuary in Australia. (b) Betsiboka River Estuary in Madagascar [Color figure can be viewed at wileyonlinelibrary.com]

geomorphological systems (Wohl et al., 2017), with implications for sediment transport (Fryirs, 2013), biodiversity (Carrara et al., 2012), vulnerability (Tejedor et al., 2015a, 2015b), and nutrient cycling (Stieglitz et al., 2003). Structural connectivity, which refers to the pattern of physical connections among landscape components (Bracken et al., 2013), can be characterized by a network topology (i.e., topological connectivity), an important constraint on how fluxes are distributed through a channel network (Tejedor et al., 2015a). Dynamic connectivity (sometimes referred to as functional connectivity Wainwright et al., 2011) describes processes controlling the magnitude and directions of fluxes (Bracken et al., 2013), and can be quantified by calculating steady-state fluxes in channel networks (Tejedor et al., 2015a). Connectivity analyses can help quantify the linkages between landscape structure and processes (e.g., Jencso et al., 2009). While the topology and self-organization of river and tidal networks (structural connectivity) are established topics (e.g., Fagherazzi et al., 1999; Horton, 1945; Rinaldo et al., 1999a, 1999b; Rodriguez-Iturbe & Rinaldo, 1997; Shreve, 1966; Strahler, 1957), recent work using techniques borrowed from graph theory for the analysis of geomorphic networks (Heckmann et al., 2015; Phillips et al., 2015) has, for example, catalyzed progress on understanding how the dynamics operating on river network topology can be interpreted to identify hotspots of geomorphological change (dynamic connectivity) (e.g., Czuba & Foufoula-Georgiou, 2014, 2015; Marra et al., 2014; Zaliapin et al., 2010).

The pioneering work of Smart and Moruzzi (1972) introduced directed channel networks and the so-called connectivity matrix to coastal deltaic environments. Recently, the structural and dynamical connectivity of channel networks in coastal systems has been reconsidered (Edmonds et al., 2011; Passalacqua, 2017; Tejedor et al., 2015a, 2015b, 2016). A recent advance introduced a delta network analysis framework based on spectral graph theory and developed a suite of metrics that characterize the structural and dynamical connectivity of river delta channel networks (Tejedor et al., 2015a, 2015b). These tools have led to important discoveries about river deltas; the evolution of channel network patterns and flux partitioning in river deltas is strongly influenced by sediment composition (Tejedor et al., 2016) and channel connectivity can influence how vulnerable a delta is to anthropogenic disturbances (Tejedor et al., 2015a, 2015b). While field, numerical, and theoretical analyses of connectivity in river deltas have led to a number of insights about structure, evolution, and transport processes (Christensen et al., 2020; Hiatt et al., 2018; Olliver et al., 2020; Passalacqua, 2017; Sendrowski & Passalacqua, 2017; Tejedor et al., 2015a, 2015b, 2016), such analyses have yet to be performed in estuaries. In this study, we extend the spectral graph analyses and metrics introduced by Tejedor et al. (2015a, 2015b) to estuarine channel networks and develop characterizations of estuaries based on the structural and dynamical connectivities.

A distinctive feature of estuaries is the change in flow direction due to tidal motion. Network analyses of river and deltaic systems often assume flow is unidirectional (e.g., Marra et al., 2014; Smart & Moruzzi, 1972; Tejedor et al., 2015a, 2015b, 2016; Zaliapin et al., 2010), but this assumption cannot be applied to estuarine environments, where flow direction changes cause temporal and spatial variation in transport processes with feedbacks influencing system geometry (Brown & Davies, 2010; Dronkers, 1986; Hoitink et al., 2003; Prandle, 2004). Additionally, estuaries may have multiple inlets and outlets, whereas previous network analyses have only considered systems with a single inlet (deltas) or outlet (rivers). Formal

frameworks exist for the analysis of tributary river network networks (originating from several upstream nodes that converge to a single outlet node) (Horton, 1945; Rodriguez-Iturbe & Rinaldo, 1997; Shreve, 1966; Strahler, 1957) and distributary networks (distributing fluxes from a single upstream node to several downstream nodes) (Smart & Moruzzi, 1972; Tejedor et al., 2015a, 2015b, 2016), but directional channel networks with the potential for both multiple inlets and outlets have not been addressed in the geosciences literature. Thus, a detailed analysis of the effects of flow direction on the channel network connectivity remains unexplored and is needed to establish a benchmark for network analysis in estuarine environments.

There are several gaps in the current state of knowledge of estuarine systems that network analyses may help address. Fluvial inflows, geomorphology and lithology, marine influences, and anthropogenic impacts differ considerably among the estuaries around the world (Kennish, 2002), and the interplay of these forces influences the structure and dynamics of estuarine channel networks. A wealth of literature exists regarding the convergent estuary shape as a function of allogenic forces (e.g., Prandle, 2004; Savenije, 2015; Townend, 2012), but our understanding of internal patterns in estuary morphology, especially the channel network, is less established. Progress has been made in quantifying the tidal bar dimensions in alluvial estuaries (Leuven et al., 2016, 2017) as a function of total estuary width, tidal prism, and hydraulic geometry; the geometry of the bar can be related to the braiding index of the channel network. However, measures like the braiding index do not quantify connection among channels. Additionally, physics-based numerical models that qualitatively reproduce channel and shoal patterns in estuaries (Lanzoni & Seminara, 2002; Townend, 2012; Van der Wegen & Roelvink, 2012) have improved our understanding of processes and emergent patterns in estuarine morphodynamics. Recent studies (e.g., Hiatt et al., 2020; Sonke et al., 2021, this issue; van Dijk et al., 2019) have used algorithmic channel detection to develop networks for geomorphological analysis in estuaries using networks, but using formal graph theory on estuarine networks remains unexplored. Accordingly, we still lack quantitative measures to properly compare and quantify patterns in real-world estuarine channel networks that could be used to validate numerical and physical experiments of estuarine morphodynamics.

In this paper, we aim to deepen the understanding of large-scale estuarine structure and dynamics by characterizing channel network connectivity in several estuaries around the world and through comparisons with schematized network structures. We do so by extending the work of Tejedor et al. (2015a, 2015b) to estuarine systems and examine the robustness of their measures describing structural and dynamical connectivity in a multidirectional environment. This work helps establish a benchmark for the structure of and dynamics operating on estuarine channel networks.

2 | BACKGROUND

2.1 | Overview of network analysis

Networks (or graphs) are mathematical representations of groups of items (like people, airports, or animals) and the relationships among those items (like friendships, flight paths, or predator–prey interactions). The network structure comprises nodes, which represent the items, and links, which represent pairwise relationships between the items. Systems that can be modeled as networks are seemingly limitless and the application of network theory is abundant across scientific disciplines (Watts, 2004). The study of networks is referred to as network analysis (or graph theory in the mathematical community). This paper is concerned with the analysis of channel networks in estuarine systems, so we limit our overview of networks as they specifically relate to geomorphology and hydrology. Readers interested in a more general discussion of networks are directed to general review articles and textbooks (Albert & Barabási, 2002; Newman, 2003, 2010; Wohl et al., 2017).

Broadly speaking, networks in the geosciences can be placed in one of two categories (Dale & Fortin, 2010; Heckmann et al., 2015): *spatial networks*, in which items have some type of spatial relationship often characterized by the flux of mass or energy; or *non-spatial networks*, in which items and their relationship have no intrinsic spatial characteristics and are generally linked by functional or process-based relationships. Analyses of non-spatial networks may include, for example, the processes involved in weathering susceptibility, ecohydrological process networks (Ruddell & Kumar, 2009a, 2009b), and sediment cascades (Heckmann & Schwanghart, 2013). Examples of spatial networks include rivers (Hiatt et al., 2020; Horton, 1945; Rodriguez-Iturbe & Rinaldo, 1997; Shreve, 1966; Strahler, 1957) and delta channels (Passalacqua, 2017; Tejedor et al., 2015a, 2015b), earthquake locations (Abe & Suzuki, 2004), and hydrological connectivity (Pringle, 2003). Networks can be either *undirected* or *directed*; directed networks have directions assigned to each link, whereas the links in undirected networks do not. Channel networks are generally analyzed as directed systems, since there is a direction associated with the transport of material. Our study is focused on the directed spatial networks (i.e., the channel networks) found in estuaries.

2.2 | Spectral graph theory

We apply the graph theoretic approach of Tejedor et al. (2015a, 2015b) to analyze estuarine channel networks. In this section, we detail the mathematical manipulation of the adjacency matrix using a slight modification of the methods developed by Tejedor et al. (2015a, 2015b). These operations were performed to generate the results in the main body of the paper.

Spectral graph theory relies on the manipulation of the adjacency matrix A and the so-called directed Laplacian matrix L (Tejedor et al., 2015a, 2015b). The topology of a network can be conveniently represented by the adjacency matrix A, which is a binary matrix in which rows and columns represent nodes, and the matrix entries indicate the presence of links connecting nodes (Figure 2a,b). In a directed network, the adjacency matrix is asymmetric and a matrix entry a_{uv} represents the link directed from node v to node u. The channel topology may also be weighted; weights could represent channel geometry or the strength of the relationship between nodes. A weighted adjacency matrix has weights w_{uv} to represent the strength of the connection directed from node v to node u, replacing the one entry in the unweighted adjacency matrix.

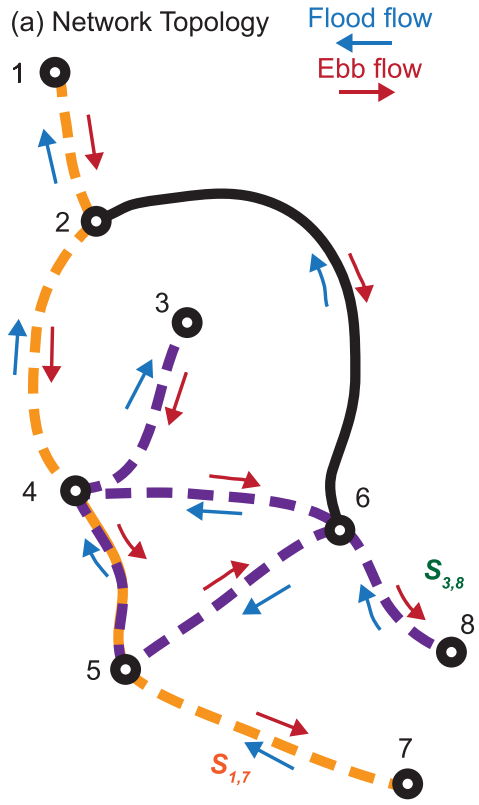

(b) Adjacency matrix

	1	2	3	4	5	6	7	8
1	0	1	0	0	0	0	0	0
2	1	0	0	1	0	1	0	0
3	0	0	0	1	0	0	0	0
4	0	1	1	0	1	1	0	0
5	0	0	0	1	0	1	1	0
6	0	1	0	1	1	0	0	1
7	0	0	0	0	1	0	0	0
8	0	0	0	0	0	1	0	0

(c) Steady State unweighted flux

	1	2	3	4	5	6	7	8
1	0	7/12	0	0	0	0	0	0
2	1/2	0	0	5/12	0	1/6	0	0
3	0	0	0	5/12	0	0	0	0
4	0	1/4	1/2	0	2/3	1/6	0	0
5	0	0	0	3/8	0	1/6	1/2	0
6	0	1/4	0	3/8	3/16	0	0	1/2
7	0	0	0	0	3/16	0	0	0
8	0	0	0	0	0	13/16	0	0

FIGURE 2 Summary of an idealized network depicting subnetworks, topology, and the steady-state flux in both the flood and ebb directions. (a) Network topology of the idealized network. The arrows along each network edge represent the direction of flow in the flood (blue arrows) and ebb (red arrows) directions. The dashed lines represent the links belonging to two different subnetworks: $S_{1,7}$, which contains all links through which material can flow between nodes 1 and 7 (orange dashed line), and $S_{3,8}$, which similarly contains all links between nodes 3 and 8 (green dashed lines). Subnetwork $S_{3,8}$ has two alternative paths between nodes 3 and 8 due to the presence of a looped section of the network between nodes 4 and 6. Subnetworks are unchanged by the direction of the flow. (b) Adjacency matrices for the network in (a). The matrix shown here represents two adjacency matrices: one in the ebb direction (A_{ebb}), with the red squares representing links that have flux present in the ebb direction, and one in the flood direction (A_{flood}), with blue squares representing the same for the flood direction. For each adjacency matrix, only one direction is considered and the fluxes in the other direction are not included (i.e., the entries for the flood direction depicted here are actually zeroes for A_{ebb} and vice versa). (c) Fraction of the unweighted steady-state flux in each link for the ebb (red) and flood (blue) directions following the same syntax as in (b) [Color figure can be viewed at wileyonlinelibrary.com]

The adjacency matrix succinctly summarizes information about the hierarchy of the network (the links between upstream and downstream nodes) from which the in- and out-degree matrices (D^{in} and D^{out}, respectively) can be constructed, where the in or out degree is defined as the number of links directed to or from a node, respectively. Thus, in matrix form, the degree matrices have non-zero entries only on the matrix diagonal. The in- and out-Laplacian matrices are defined as follows:

$$L^{in(out)} = D^{in(out)} - A, \tag{1}$$

where L stands for the Laplacian matrix and the superscript indicates whether the *in* or *out* degree matrix is considered. The Laplacian is useful because the properties of its null space can be used to describe the structural and functional connectivity of a directed graph (Tejedor et al., 2015a).

The eigenvector x of the matrix L is related to the eigenvalue λ as follows:

$$Lx = \lambda x, \tag{2}$$

where $x = [x_1, \ldots, x_N]$ and λ is a scaling constant. The unweighted steady-state flux is the eigenvector that spans the null space of L (or, in other words, when $\lambda = 0$) (Tejedor et al., 2015a). Weighted steady-state fluxes can then be determined as follows:

$$F_i = \sum_j w_{ij} F_j, \tag{3}$$

where F_i is the steady-state flux in node i, w_{ij} is the weight along the link connecting node j to node i (in that direction), and F_j is the flux at node j. The fluxes at link vu are then assigned as $F_{uv} = F_v w_{uv}$ (e.g., Figure 2c). In this paper, fluxes in both the ebb and flood directions are independently considered. In other words, a unique adjacency matrix is developed for each direction (A_{flood} and A_{ebb}) and the steady-state fluxes are calculated for each of these adjacency matrices. Steady-state fluxes represent mathematical properties of the network structure and geometry. Flow partitioning at a bifurcation (i.e., a node) through downstream channels is proportional to channel widths (Bolla Pittaluga et al., 2003; Kleinhans et al., 2013; Wang et al., 1995; Zolezzi et al., 2006), and thus the calculation of width-weighted

steady-state fluxes herein can provide an insight into flux allocation in remotely sensed networks.

A contributing subnetwork is the set of nodes that drain to node *u*. Subnetworks are identified in the network topology so that metrics can be calculated on each subnetwork (Tejedor et al., 2015a, 2015b). In deltaic systems studied by Tejedor et al. (2015a, 2015b), there is only one inlet (i.e., the delta apex), so subnetworks are uniquely identified by the outlets (e.g., Figure 2a). However, in the estuarine systems studied here, there can be multiple inlets and outlets, so each subnetwork is uniquely defined by the inlet–outlet pairing and not simply by the outlet. Therefore, the estuarine networks studied here potentially have a large number of subnetworks relative to the number of links/nodes as compared to deltaic systems.

3 | METHODS

We apply a series of metrics developed by Tejedor et al. (2015b) to estuary channel networks and compare the results from real-world estuaries to the those from schematic estuary networks that are intended to represent end-member cases of multi-channel estuarine networks observed on Earth. Most of the metrics are applicable to estuaries with multiple outlets, but not to estuaries with a single outlet channel, because most metrics rely on comparing measures in one subnetwork to another. In this section, we provide an overview of the network metrics followed by a description of the schematic estuaries and the channel network extraction from satellite imagery for real-world estuaries.

3.1 | Network metrics

A suite of descriptive metrics are considered: the number of alternative paths (NAP), the resistance distance (RD), the link sharing index (LSI), the flux sharing index (FSI), and the leakage index (LI). The first three metrics (NAP, RD, and LSI) are measures of structural connectivity and attempt to quantify the structure of the network. The remaining metrics (FSI and LI) are measures of dynamic connectivity that characterize the behavior of fluxes (F_{uv}) as they are partitioned throughout the network. Because estuarine fluxes are bidirectional due to tides, we apply the network metrics in both the flood and ebb directions by changing the designations of inlet and outlet nodes based on the perceived flow direction determined from satellite imagery.

Detailed descriptions and mathematical formulations for each metric are described thoroughly in the Supporting Information and in Tejedor et al. (2015b). Here we summarize the important aspects of each metric required for understanding the results presented in Section 3. Each metric is computed for all subnetworks within the network, and the results are presented as a distribution.

Structural connectivity measures include number of alternative paths, resistance distance, and link sharing index. The number of alternative paths (NAP) counts how many different paths a unit of flux can travel along from source to sink in a given subnetwork. The resistance distance (RD) is a measure of structural connectivity that quantifies how connected an inlet and outlet node are within a subnetwork. RD accounts for the "loopiness" of the subnetwork and the presence of significantly different alternative paths through the subnetwork. High values of RD indicate a relatively loopless path through the subnetwork, while lower values indicate numerous alternative routes through the subnetwork. The link sharing index (LSI) is a more complicated metric that attempts to quantify the level of structural overlapping among subnetworks. The LSI for a given subnetwork will be high if it shares many of its links with other subnetworks, and low if the links within the subnetwork are relatively isolated from other subnetworks. To provide a quantification of these metrics on a relatively simple network, the above structural connectivity measures are summarized in Table 1 for sample subnetworks within the network topology shown in Figure 2. Note that the structural connectivity measures do not depend on direction.

TABLE 1 Network metrics for the subnetworks delineated in Figure 2

	$S_{1,7}$		$S_{3,8}$	
	Flood	Ebb	Flood	Ebb
NAP	1	1	2	2
RD	1	1	0.89	0.89
LSI	0.56	0.56	0.55	0.55
FSI	0.38	0.75	0.58	0.25
LI	0.16	0.38	0.23	0.08

The metrics quantifying dynamical connectivity are flux sharing index (FSI) and the leakage index (LI). The FSI is the average proportion of steady-state flux of nodes within the subnetwork that arrives at the outlet. The FSI is challenging to intuit, but can be viewed as a measure indicating how much flux interaction there is between one subnetwork and the others, and the degree to which LSI influences that sharing. The LI is more straightforward and is the proportion of flux entering a node that is lost to other subnetworks. Both dynamical connectivity metrics are tabulated in Table 1 for the selected subnetworks in Figure 2.

A new metric is introduced called the directional flux ratio (DFR). The DFR is simply computed as the ratio in steady-state flux in a given network link in the flood direction to the steady-state flux in the ebb direction. Links with greater flood flux have DFR values greater than 1, while links with flood flux less than the ebb flux will have DFR values less than 1. If the steady-state fluxes in the link are completely symmetrical, DFR will equal 1.

3.2 | Schematic estuary networks

The earth sciences often rely on comparing field/laboratory results, numerical modeling, and/or remotely sensed data to theory to assess the validity of results. Unfortunately, there is no theory regarding the structure of estuarine channel networks, so we have created four schematic estuarine networks intended to represent idealized end-members of multi-thread estuarine network structure and flux partitioning. The schematic networks will serve as a benchmark for understanding the structure of estuary networks found in the field or generated in laboratory or numerical experiments. The four schematic networks with self-similar structure were created for a range of network sizes quantified by number of nodes. They include a binary

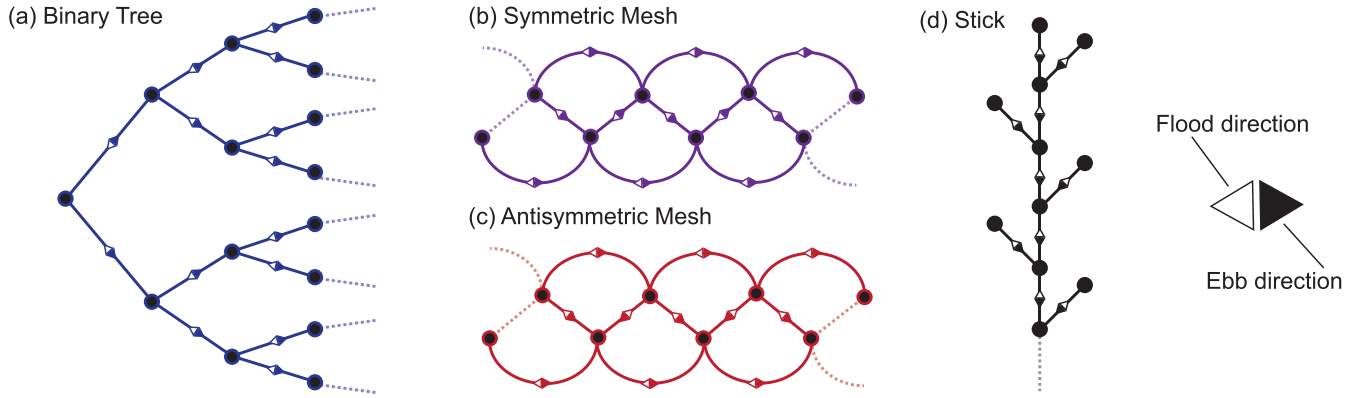

FIGURE 3 Schematic networks where circles represent nodes and lines represent links. The dashed lines represent potential links depending on network size [Color figure can be viewed at wileyonlinelibrary.com]

tree (Figure 3a), symmetric and antisymmetric meshes (Figure 3b,c), and a stick network (Figure 3d). Network metrics were computed on each schematic network for a range of network sizes determined by the range of network sizes for the networks extracted from satellite imagery (see next subsection).

The binary tree network (Figure 3a) is representative of an idealized branching system that resembles a river delta and is included to represent an end-member for delta-like estuaries that have branching systems. In the flood direction, material is fluxed from multiple inlets to a single outlet, and the opposite is true in the ebb direction. The number of subnetworks is dependent on network size. The idealized mutually evasive flood and ebb channel system that is indicative of estuaries, first conceptualized by van Veen (1950), is represented by the symmetric mesh network (Figure 3b). In the symmetric mesh, fluxes are permitted to flow along either branch at bifurcations and is structurally symmetric about its longitudinal axis. It contains four subnetworks (two inlets and two outlets) regardless of network size. This network is intended to represent a relatively wide alluvial estuary with bars (Leuven et al., 2017), as opposed to a narrow converging estuary without bars. In the channels around bars, a major fraction of the sediment in motion may tend to circulate rather than transport mainly in one direction (Jeuken & Wang, 2010). The antisymmetric mesh network is structurally similar to the symmetric mesh, but the direction of the internal links (Figure 3c) preferentially allocates flux to one side of the network (compare the direction of the vertical links in (c) and (d)). Thus, it contains only three subnetworks (two inlets and two outlets) regardless of network size. Thus it is not symmetric about its longitudinal axis and it differs in flux partitioning between the ebb and flood phase, as often found in bar-dominated estuaries. Finally, the stick network (Figure 3d) represents a simple estuary with a main branch and offshoot channels that could represent barb channels found in many estuaries or multiple tributaries entering the estuary. The structure of the stick network is similar to the binary tree, but without the tree-like branching. It idealizes a relatively simple estuary, narrower than the mesh networks, with one main channel and several dead-end branches or embayments. In the flood direction, material is fluxed from a single inlet to multiple outlets, while the opposite is true in the ebb direction. The number of subnetworks is dependent on network size.

Structural and dynamical connectivity metrics were calculated in the flood and ebb direction for each unweighted schematic network. Network sizes for each schematic network ranged from ~10 to ~600 links with the exception of the stick network. The stick network was capped at 300 links due to computing limitations.

3.3 | Real-world networks extracted from satellite imagery

Networks for 13 multi-channel estuaries and deltas were created using LANDSAT 8 satellite imagery (Figure 4). The selected estuaries span a range of latitudes, climates, river and marine influences, and anthropogenic control, and include some deltas for comparison. The acquisition date of image(s) for each system is presented in Table 2 and information including geographical coordinates, hydrography and tidal characteristics (if available), and other environmental conditions for each system is included in the Supporting Information. We utilized RivaMap (Isikdogan et al., 2015; 2017), an open source channel centerline extraction tool that utilizes a multi-scale singularity analysis (Muralidhar et al., 2012), to identify channel features from satellite imagery without the need for spectral thresholding. Networks and associated topologies were generated as follows:

1. Images were transformed using the Modified Normalized Difference Water Index (MNDWI) (Xu, 2006) to enhance the contrast between water and land pixels. The contrast in the resulting image was rescaled by applying a contrast stretch. Images containing clouds that obscured the channel network were not included in the analysis.
2. River channel centerlines were extracted using the MATLAB version of RivaMap from the transformed images.
3. Connectivity at bifurcations and confluences among channels is not maintained by RivaMap (Isikdogan et al., 2017), so connections were drawn manually using the satellite image as reference.
4. For each channel, the width was determined from the singularity index generated by RivaMap (see Isikdogan et al., 2015, for details) using the geoprocessing tools presented in Marra et al. (2014). Width was assigned as an attribute to each channel. The length

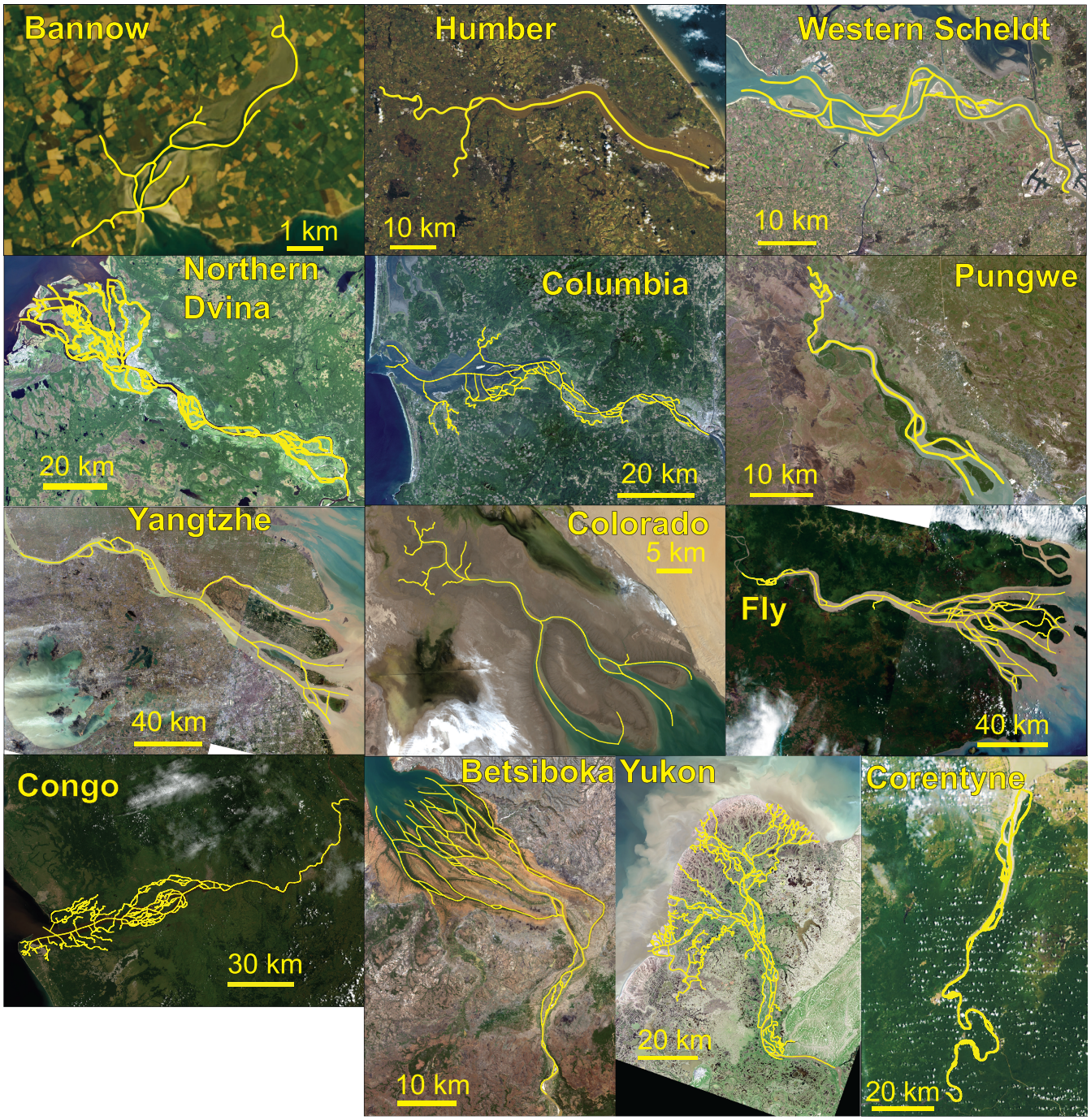

FIGURE 4 Satellite images with extracted channel networks for 13 estuarine and deltaic systems. Note that each image has its own scale bar. Images were compiled using LANDSAT 8 images from the USGS Earth Explorer [Color figure can be viewed at wileyonlinelibrary.com]

of the channel was also determined using GIS (geographic information system).

5. After generating the networks, flow directions were assigned to the width-weighted adjacency matrix based on the perceived flow direction from satellite imagery.

Steady-state fluxes were calculated in both the flood and ebb directions and were weighted by the link widths determined from satellite imagery. Fluvial inputs and tidal ranges were not considered when determining the steady-state fluxes. Thus, the results represent a most basic case of the network considering only topology and geometry.

4 | RESULTS

The results section is divided into results for the schematic estuaries and those from the real-world networks extracted from satellite imagery. In each subsection, the results from the network metrics calculated in both the flood and ebb directions are presented.

4.1 | Schematic networks

Distributions of network metrics were calculated for the binary tree, symmetric mesh, antisymmetric mesh, and stick networks (Figure 5).

TABLE 2 List of LANDSAT 8 scenes

Location	Acquisition date	Abbreviation
Bannow	08/29/2016	Ba
Betsiboka	08/11/2016	Be
Columbia	08/19/2016	Cb
Congo	03/03/2015	Cg
Colorado	04/14/2016	Co
Corentyne	10/06/2015	Cr
Fly (East)	10/12/2016	Fl
Fly (West)	09/28/2014	Fl
Humber	02/23/2016	Hu
Northern Dvina	08/21/2015	Nd
Pungwe	07/09/2015	Pu
Western Schedlt	10/31/2016	We
Yangtze (East)	08/03/2016	Ya
Yangtze (West)	01/01/2016	Ya
Yukon	05/31/2016	Yu

Structural connectivity measures include RD, LSI, and NAP. Resistance distance generally decreases with increasing network size, which is quantified by the number of links within the network (Figure 5a). Structural connectivity measures are not affected by network direction, so the results are presented independent of direction. The median value for RD for all schematic networks except for the symmetric mesh is 1 regardless of network size. For the symmetric mesh, RD decreases with network size until asymptotically approaching a value of 0.4. Though the median value of the antisymmetric mesh (red diamonds in Figure 5a) is 1, the lower range of values exactly matches that of the symmetric mesh. Both the binary tree and stick networks have RD values of 1 for every subnetwork because there are no alternative paths in these networks.

The median NAP in the binary tree, antisymmetric mesh, and stick networks all have median values of 1, and the range in NAP increases with network size for the antisymmetric mesh (Figure 5b). Conversely, the NAP for the symmetric network exponentially increases with network size due to birfurcating and rejoining structure of the network. The absence of alternative paths is expected for binary tree and stick networks, because there are no loops present. The two mesh networks have numerous loops, but the median value of 1 for the antisymmetric mesh is due to the preferential connection to one side of the network.

The LSI has a positive relationship with network size, and each network type tends to asymptotically approach a maximum value (Figure 5c). All metrics approach an asymptotic value as the number of links increases. The binary tree network does not begin to level off within network sizes tested, but should approach 1 as the number of links goes to infinity (Tejedor et al., 2015b). The binary tree subnetworks all have the same LSI value at a given network size, due to the fractal structure of the network. The LSI for symmetric mesh approaches a maximum value of about 0.75 from a minimum value of 0.6 calculated at small network sizes. The range in values about the median LSI is small for the symmetric mesh, and it decreases with network size. The LSI for the antisymmetric mesh has a smaller median and larger range than the symmetric mesh. The stick network has an LSI that rapidly approaches 1 at a network size of 300. For the range, the stick network also has very low values of LSI, which are due to very small subnetworks that begin very close to the network outlet, and thus share very few links with other subnetworks.

The dynamical connectivity measures calculated for the schematic networks are the LI, FSI, and DFR (Figure 5d-f). The median LI ranged from zero to 0.5 for each of the schematic networks (Figure 5d). Each subnetwork in the binary tree (ebb direction) has a leakage index of 0.5, because fluxes are split evenly at every bifurcation in the unweighted network. The stick network in the flood direction also has a median value of 0.5 for the same reason. In the flood direction, values of LI are zero for the binary tree. In the ebb direction, LI in the stick network has a median of zero because each subnetwork shares a common outlet node. The median LI values of both mesh networks quickly approach zero, and the range about the median decreases with increasing network size for both. The LI distribution is unaffected by network direction for both mesh networks because the adjacency matrices are functionally equivalent in each direction.

The FSI exhibits wide-ranging behavior across the network types and directionality (Figure 5e). The binary tree network has high values of FSI in the ebb direction because the flux is split evenly at each successive bifurcation. Thus, there is increasing overlap of fluxes among subnetworks in the upstream portions of the network as the number of edges increases. In the flood direction, FSI is expectedly zero at all network sizes because no material is fluxed from one subnetwork to another. The symmetric mesh has a median FSI of 0.5 for all network sizes, while the antisymmetric mesh has progressively lower median values of FSI with network size. The variability in FSI across subnetworks is very high in the antisymmetric network, with some subnetworks reaching an FSI value of about 1 at larger network sizes. The stick network shows significant disparity in FSI depending on direction, with the ebb direction yielding FSI values of zero and and approaching 1 in the ebb and flood directions, respectively.

Each idealized network has a DFR median that does not change with network size since the networks are generally symmetric, except for the stick network. The antisymmetric mesh network DFR distribution does exhibit significant variability as the size of the network increases, since the location of flux concentration changes with flow direction. Because of the mirrored nature of the antisymmetric network structure, the DFR rapidly approaches very large numbers, because of the preferential flux of material to one side of the network. The stick network fluxes are biased toward ebb fluxes, because the system acts as a tributary in the ebb direction, greatly increasing flux values along the main stem relative to the flood direction.

4.2 | Real-world networks

We calculate the resistance distance (RD), link sharing index (LSI), flux sharing index (FSI), leakage index (LI), number of alternative paths (NAP), and the directional flux index (DFI) for each estuary network. For the metrics related to the structure of the network (i.e., RD, NAP, and LSI), there is a correlation with the number of links in the network (Figure 6a,b,c). Larger networks tend to have lower median values and higher variability in RD than do smaller networks. There is appreciable scatter about the overall trend of decreasing RD with increasing network size. This result is intuitive, as networks with more links tend

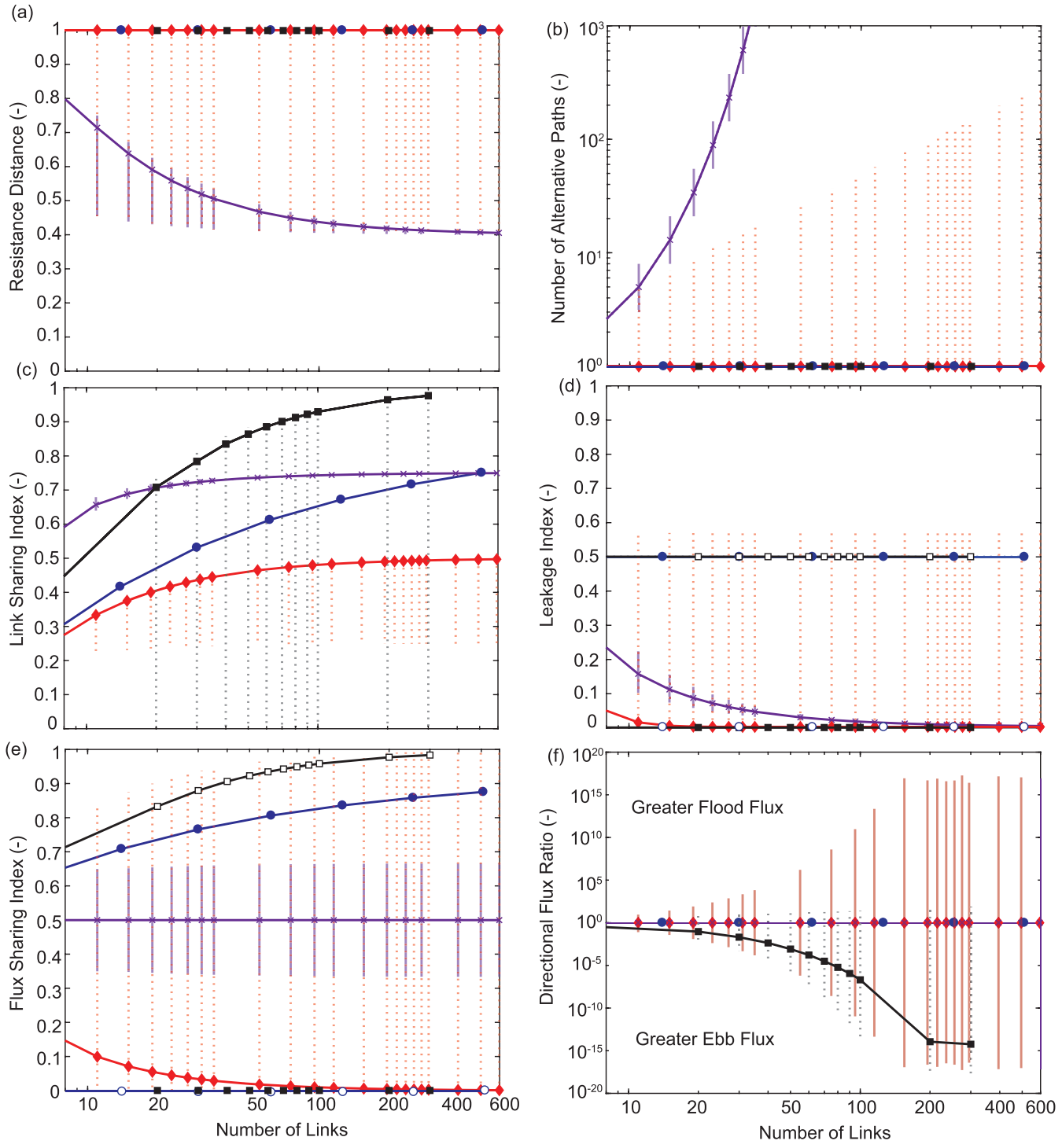

FIGURE 5 Structural (a–c) and dynamical (d–f) connectivity metric results for schematic networks over a range of network sizes. The distributions for each metric are summarized by a median value and the 5th and 95th percentiles (indicated by vertical lines). Open symbols represent flood direction and filled symbols represent ebb direction. Each network is represented by a unique symbol and color (corresponding to Figure 3): binary tree (blue circles); symmetric mesh (purple x symbols), antisymmetric mesh (red diamonds), stick (black squares) [Color figure can be viewed at wileyonlinelibrary.com]

to contain more loops, which causes a decrease in RD. However, there is considerable variability in the presence of loops among the networks. Network size and NAP appear to be correlated (Figure 6b) but there are notable deviations from this trend (e.g., the Congo system). Larger networks also tend to have greater variability in NAP than do smaller networks. The opposite behavior is true for the LSI, which tends to increase as the network gets larger. The Colorado (Co) network LSI distribution is higher than similarly sized networks, which is probably due to the presence of many tidal channels that connect to the main estuarine channel, which facilitates a high degree of link sharing among the subnetworks. Considerable variability in the value of LSI exists for the Yukon network (Yk), which is likely due to its very large number of subnetworks.

Dynamical connectivity metrics (LI, FSI, and DFR) do not appear to have a positive correlation with network size (Figure 6d–f). Median values of LI are typically below 0.2, and no subnetworks had LI values

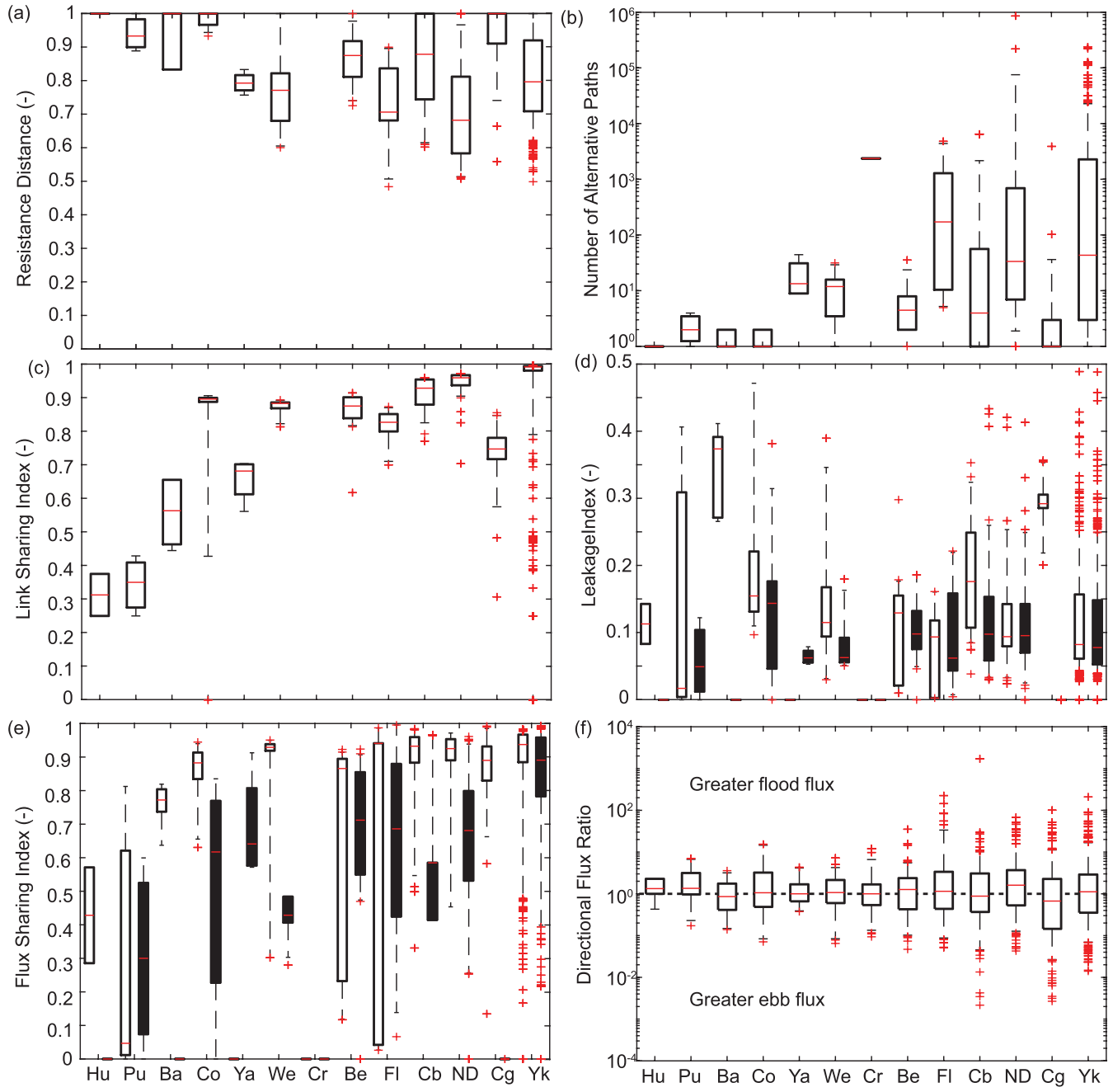

FIGURE 6 Summary of the network metrics evaluated for the networks shown in Figure 4 using a box and whisker plot arranged in order of increasing network size. Median values are indicated with a red line plotted inside the box delineating the 25th and 75th percentiles. The whiskers extend to the 5th and 95th percentiles. Red crosses thus indicated outliers. The *x*-axis in all panels is organized by increasing network size. The metrics show are: (a) resistance distance (RD); (b) number of alternative paths (NAP); (c) link sharing index (LSI); (d) leakage index (LI); (e) flux sharing index (FSI); and directional flux ratio (DFR). Structural connectivity metrics (RD, LSI, and NAP) are calculated independent of direction, and dynamical connectivity metrics (LI, FSI, and DFR) depend on direction. For LI and FSI, white indicates the flood direction and black indicates the ebb [Color figure can be viewed at wileyonlinelibrary.com]

greater than 0.5 (Figure 6d). However, there is significant variability in the LI distributions in both the flood and ebb directions and no correlation with network size or directionality.

Median FSI tends to increase with network size, but there is significant variability (Figure 6e). For many of the networks, the median FSI is greater in the flood direction than in the ebb direction. The null hypothesis of equivalent medians between the flood and ebb FSI distributions for a Wilcoxon rank-sum test at the 5% significance level was run and rejected for half of the networks analyzed (Bannow, Yangtze, Western Scheldt, Columbia, Northern Dvina, Congo, Yukon). The null hypothesis was not rejected for the other networks (Humber, Pungwe, Colorado, Corentyne, Betsiboka, and Fly). Thus, larger networks seem to have a more significant disparity in median FSI.

The Corentyne network has values of zero for RD, LSI, LI, and FSI because the network only contains one subnetwork. All of these metrics rely on interactions with other subnetworks and are thus zero. The NAP depends on the presence of loops in the system, which are present in the Corentyne.

All of the real-world networks studied have median DFR values very close to 1 (Figure 6f). Variability about the median tends to increase with increasing network size, and there are many more links that have DFR values that lie outside the 25th and 75th percentiles.

5 | DISCUSSION

5.1 | Comparison of real-world and schematic networks

The results from the real-world networks are compared to the distributions of results from the schematic networks to contextualize the structural and dynamical connectivity of estuaries in this study (Figure 7). The placement of the distributions for each natural network is indicative of the structural and dynamical elements of the network, and the proximity to the distributions of schematic networks is interpreted by how similar the real-world networks are to the end-members represented by the schematic networks. For discussion clarity, the region between the 25th and 75th percentiles for each real-world network is referred to as the inter-quartile distribution (IQD) and the region bounded by the 5th and 95th percentiles is called the P5–P95 envelope.

For the real-world networks, the IQDs of all metrics are bound by the medians of each schematic network and fall within the the P5–P95 envelope for the range of network sizes tested (Figure 7). This implies that the schematic networks generated for this analysis are reasonable representations of end-members of estuarine structural and dynamical connectivity. The IQDs of RD all lie within the P5–P95 envelope for the antisymmetric mesh and plot well outside the P5–P95 envelope of the symmetric mesh (Figure 7a), indicating that the idealized mutually evasive flood and ebb channel structure of the symmetric mesh may not be reflected in the structure of real-world estuarine systems. Supporting this argument is the significant deviation in the IQDs for NAP compared to the P5–P95 envelope for the symmetric mesh (Figure 7b). The NAP median in real networks is always smaller than that of the idealized symmetric mesh, indicating that real estuaries contain fewer looping structures than a mesh. Some NAP medians are equal to zero, indicating that highly asymmetric structures or tree-like structures (stick or binary tree) can comprise a significant portion of estuarine networks. The LSI for natural networks generally plots between the binary tree and stick medians (Figure 7c). At larger network sizes, the influence of stick-like network structures, such as the presence of barb channels (Dalrymple & Choi, 2007; Leuven et al., 2016, 2018; Robinson, 1960), leads to very high values of LSI. In general, the IQDs for the real-world networks do not plot near the LSI distribution for the antisymmetric mesh, which suggests that the structural connectivity of the studied estuaries is fairly balanced across subnetworks. However, it is clear from the variability place of the real-world IQDs, relative to the distributions of the schematic networks, that no one metric can completely capture sweeping trends in structural connectivity across the systems studied (Figure 7a–c).

The IQDs for the LI all have values less than 0.4 (Figure 7d), indicating that the flux distribution in the networks is somewhere in between the behavior for tree-like networks (binary tree and stick medians plot at 0.5) and mesh-type networks (symmetric and antisymmetric mesh medians approach zero). The IQDs for the FSI span a wide range of values for both the real-world and schematic networks but the IQDs fall within the P5–P95 envelope of most of the schematic networks (Figure 7e). Some networks have very high values in the IQD of FSI that are similar to the flood-direction FSI median for the stick network, which suggests tidal structures may play a large role in the partitioning of fluxes in these systems. Indeed, the anomalously high LSI IQD values for the Bannow and Western Scheldt (Figure 6c) systems is likely due to stick-like tidal subnetworks nested within the overall network (Figure4), which is also manifested through stick-like behavior in the partitioning of fluxes in the flood direction (Figures 6e and 7e).

Because no one measure of either structural or dynamical connectivity appears to fully capture the structure or dynamics of the analyzed networks, we view the data from Figure 7 in three parameter spaces defined by selected metrics (Figure 8). Doing so should provide further insight into how real-world networks relate to the end-member schematic networks. We compare two measures of structural connectivity: RD and LSI (Figure 8a). In the RD-LSI parameter space, the medians for most networks lie outside the P5–P95 envelope of the schematic networks. Most networks occupy the parameter space between the symmetric mesh and binary tree or stick medians, indicating that the systems studied likely exhibit a combination of the characteristic structural of an idealized flood–ebb channel configuration (e.g., van Veen, 1950) and branching channel structures that may be indicative of deltaic (binary tree) or tidal (stick) structures. Note the structural connectivity measures do not depend on flux direction.

The real-world networks mostly occupy the same space when comparing dynamical connectivity measures (LI and FSI; Figure 8b) but the directionality of the stick and binary tree networks factor in the interpretation. In this parameter space, the real-world medians lie largely between the medians for the symmetric mesh and binary tree ebb direction and the stick flood direction. Due to their branching nature in the direction of the flux, the dynamical connectivity of the binary tree ebb and stick flood are indicative of fluxes being broadly distributed across subnetworks. In this comparison, many networks have values of zero in the ebb direction (Congo, Humber, Corentyne, and Bannow), because the system converges to a single outlet in the landward portion of the network. The opposite is true for the delta-like Yangtze.

In the parameter space of structural to dynamical connectivity, the median FSI and LSI values for each real-world network lies within a region between the medians of the flood/ebb symmetric mesh and the stick (flood) and binary tree (ebb) distributions (Figure 8c, compare open and closed symbols with shaded areas). In all three parameter spaces tested, the real-world networks exhibit branching structures likely nested within the classical symmetric mesh structure. Thus, the majority of networks tend to partition fluxes with characteristics both of the symmetric mesh, indicating mutually evasive flood and ebb channels as in van Veen (1950) and Leuven et al. (2016), and a branching network that more broadly distributes flux across subnetworks than the symmetric mesh, which points towards either tidal or delta-like channel network structures as in Tejedor et al. (2015b). Visual inspection shows that most of the networks indeed have multiple outlets (Figure 4) and, as such, a tendency towards the binary tree is obvious. On the other hand, the network analysis also points at flood/ebb asymmetry, which is a strong indication that the

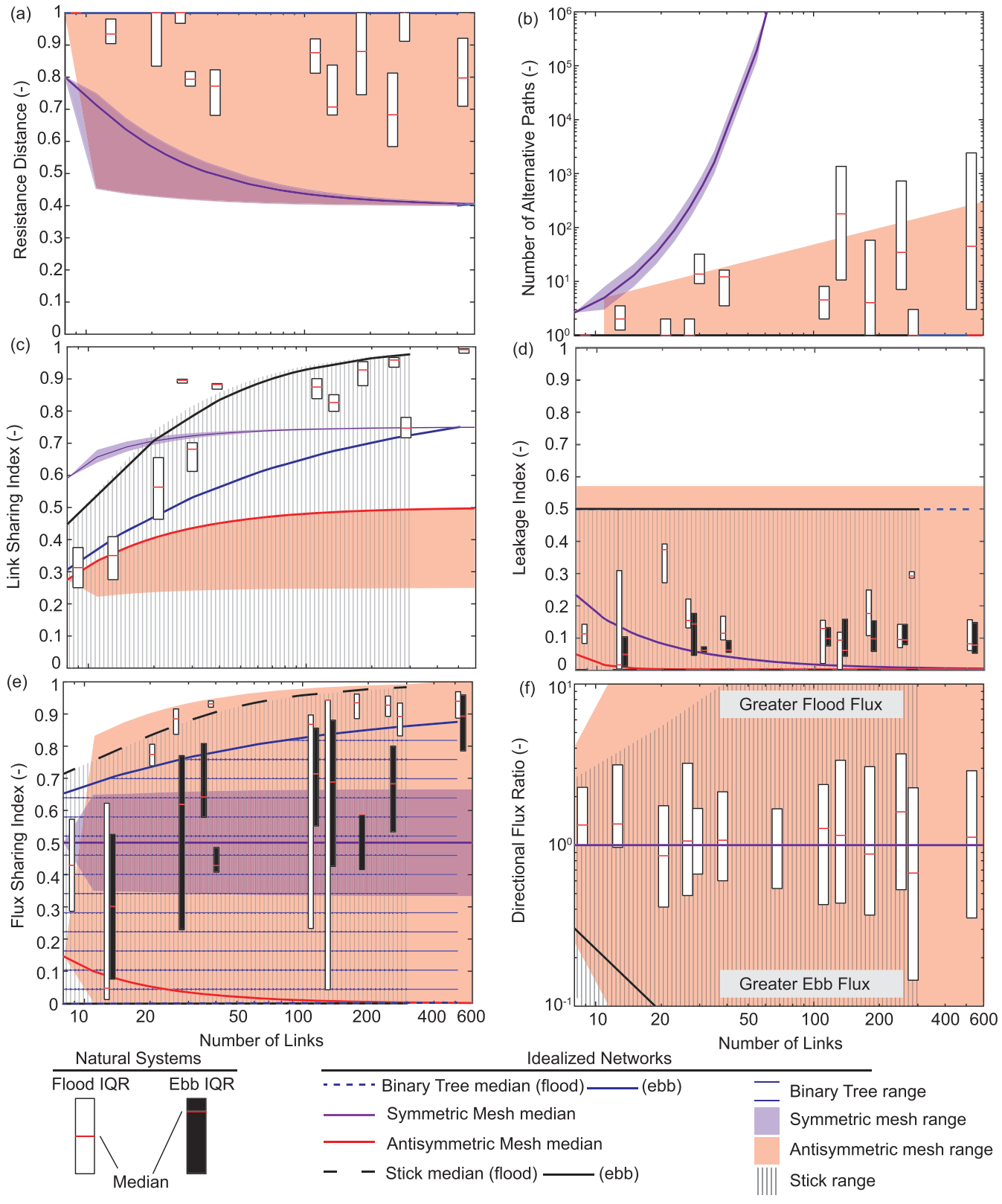

FIGURE 7 Summary of real-world network metric distributions compared to idealized networks. The median and 25th and 75th percentiles are presented as a box plot for each real-world network in both flood (white) and ebb (black) directions, if applicable. For the schematic networks, the median is drawn as a solid line and shaded areas are bounded by the 5th and 95th percentiles. Each metric is plotted against the number of links in the network, which is a proxy for network size (provided in the Supporting Information) and is of the same order as Figure 6. For figure clarity, the whiskers and outliers of the real-world networks shown in Figure 6 are not shown [Color figure can be viewed at wileyonlinelibrary.com]

mechanisms causing mutually evasive flood and ebb channels operate also in systems of multiple outlets, which would not easily be detected by simpler and visual inspection.

Dynamical connectivity measures, particularly the FSI, tend to have higher median values than the ebb direction (Figure 8b,c), which indicates that fluxes are more broadly partitioned across the network

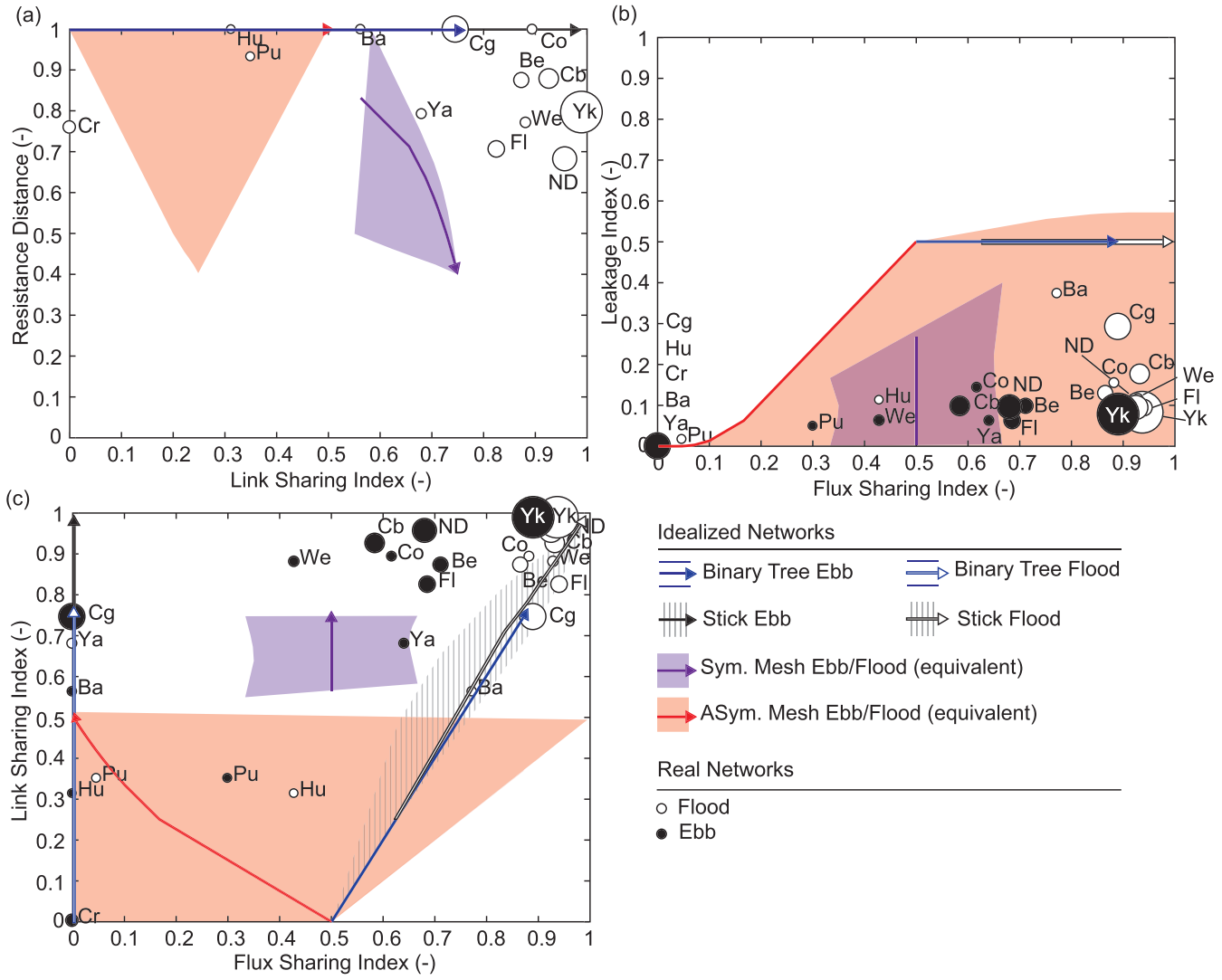

FIGURE 8 Comparisons among structural and dynamical connectivity measures for the schematic and real-world networks plotted in several parameter spaces: (a) RD and LSI; (b) LI and FSI; and (c) LSI and FSI. For each real-world network, the median is plotted and the size of the dot indicates the relative size of the network (number of links). For the idealized networks, the lines represent median values, while the arrow indicates the direction of increasing network size. The shaded region is bounded by the 5th and 95th percentiles for each idealized network distribution. In several cases, there is no shading for the binary tree or stick networks, because there is no variability in the metric value among subnetworks for a given direction (e.g., FSI and LI for binary tree ebb and stick flood). Open symbols indicate the flood direction, while closed symbols represent the ebb direction (arrows for idealized networks and dots for real networks) [Color figure can be viewed at wileyonlinelibrary.com]

structure in the flood direction than in the ebb direction. The interpretation is supported by the proximity of flood direction medians to the binary tree (ebb) and stick (flood) medians in the LSI–FSI parameter space, but there is significant scatter. Nevertheless, this appears to support the concept of circulating sand currents in estuaries with predominant sediment transport onto shoals and into barb-like channels in the flood direction and sediment transport in downstream concentrated in ebb-dominated main channels (Brown & Davies, 2010; Dronkers, 1986; Leuven et al., 2016; van Veen, 1950). The tendency of one, or a few, ebb-dominant channels and flood dominance of the shoals and bars stems from the phase difference between tidal water-level fluctuation and tidal currents and is common in many tidal systems (e.g., Braat et al., 2017; Brown & Davies, 2010; Wang et al., 2002).

Qualitative zonations were developed based on interpretations of the LSI and FSI and applied to the LSI–FSI parameter space to provide context for values of real-world networks (Figure 9). Networks with high medians of LSI and FSI contain many structural elements (links) that are shared among subnetworks and thus have broad flux distribution among those subnetworks. Most of the networks studied lie within this region of the LSI–FSI parameter space. This is also true of a data set of only river deltas as analyzed by (Tejedor et al., 2015b) and is unsurprising because many of the systems studied here have branching delta-like structures, but also carry the signature of flood–ebb asymmetry and mutually evasive channels, which create many opportunities for flux sharing to the presence of loops. Several networks also exhibit high medians of LSI and low medians of FSI (Figure 9), which is generally indicative of a structure with limited outlets in one direction, causing flux localization with limited capacity for transfer among subnetworks. This is found in the ebb direction for the Congo, Western Scheldt, and Bannow, which all carry some characteristics of the tidal structure of the ebb direction stick network, and the flood direction for the binary tree-like network of the Yangtzhe. Networks with low LSI and FSI medians are the Humber,

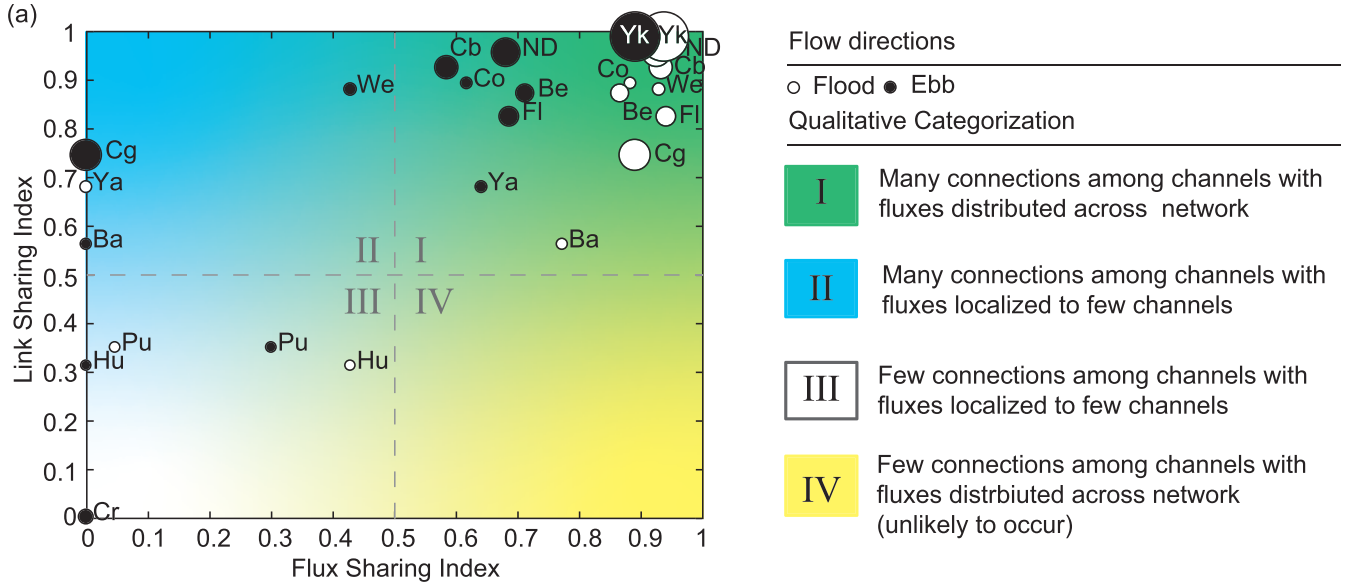

FIGURE 9 A qualitative categorization based on interpretations of the structural link-sharing index and the dynamical flux-sharing index. Real-world network medians are plotted over the qualitative categories as circles. Marker size indicates the relative network size, and white and black circles represent flood and ebb directions, respectively [Color figure can be viewed at wileyonlinelibrary.com]

Pungwe, and Corentyne. These networks have very few connections among subnetworks because they have very few channels overall, and there is limited opportunity for flux to be partitioned among subnetworks. Finally, no networks studied lie within a region of high FSI and low LSI (Figure 9). This is expected, because it is highly unlikely that a network would form in such a way to facilitate significant flux partitioning among subnetworks when limited structural connections are available.

The results in this study indicate that larger estuary networks tend to have larger median values of LSI (Figure 6c), though there is significant scatter in LSI across subnetworks at large network sizes. In general, networks with greater numbers of links (i.e., larger) tend to have more loops and interconnectedness among the various subnetworks, which leads to large values of LSI. This was also found by Tejedor et al. (2015b) for deltaic networks. The high LSI for large networks in this study indicates that estuarine networks tend to self-organize in such a way as to maximize the structural connectivity within the channel network. Because the networks presented in this study were extracted from satellite imagery, the self-organization of channels yielding high LSI values also means that the estuary bars are developing into predominantly subaerial features that can be distinguished from water in a satellite image (Figure 4). This interpretation is intuitive for larger networks, because the size of the system allows for appreciable channel–shoal patterns (Leuven et al., 2016; Van der Wegen & Roelvink, 2012) that are larger than the resolution of satellite imagery. Two systems tend to deviate from this behavior: the Corentyne (Cr) and the Congo (Cg). These networks tend to be more similar to braided systems than the other estuaries in this study (Figure 4) and have a limited number of inlets/outlets.

5.2 | Limitations and future directions

A significant limitation to the use of spectral graph theory developed by Tejedor et al. (2015a, 2015b) for estuarine network analysis is the requirement of the estuarine network to have multiple inlets and outlets to generate many of the network metrics used in this study. Under the assumptions of the graph theory used to calculate these metrics, which were originally intended for deltaic distributary networks, the system must comprise at least two subnetworks in order to generate a distribution of RD, LSI, LI and FSI because the metrics are calculated on a subnetwork to subnetwork basis. This limitation is exemplified by our results for the Corentyne network (Figure 6), which had trivial values of RD, LSI, LI, and FSI because the system had only one inlet and one outlet. Many alternative paths were identified and the flux ratios depending on direction were quantified (Figure 6b and f, respectively) because those metrics are independent of the subnetwork requirement. Thus, the selection of estuaries that could be analyzed was limited to relatively large estuaries with multi-thread channel networks that were resolved at the resolution of satellite imagery. The use of network analysis for estuaries would benefit from the development of targeted metrics based on graph theory that can handle "chain-like" systems with only one inlet and one outlet. Such an advancement would likely benefit our understanding of braided river networks and other "chain-like" directed Earth system networks that have relatively few available graph theoretic approaches compared to undirected networks (Heckmann et al., 2015; Phillips et al., 2015).

Considerable focus in estuarine research has been placed on the importance of tidal asymmetry and its relations to estuarine geometry and net sediment transport (Brown & Davies, 2010; Dronkers, 1986; Friedrichs & Aubrey, 1988; Kang & Jun, 2003; Prandle, 2003). General conclusions are that ebb–dominance causes a net sediment loss from the estuary, resulting in an increased channel depth; flood dominance causes net sediment influx, resulting in sediment accumulation and a decreased average depth. Estuaries may alternate between these phases (Brown & Davies, 2010), enlarge, or silt up, depending on fluvial and coastal sediment supply (de Haas et al., 2018). Since channels are the primary conveyor of momentum and sediment in

estuaries, the channel network connectivity and the dynamics operating on the network are potentially indicative of the processes occurring in the channel network and on the shoals and bars flanking and terminating the channels. Future research on tidal asymmetry in multi-channel estuaries may benefit from using spectral graph theory to calculate steady-state fluxes in both the flood and ebb directions, then by applying metrics such as DFR that directly quantify asymmetry on individual network links. However, this approach is currently limited by a lack of network-scale flux measurements in estuaries due to logistical or instrumentation constraints. Validated numerical modeling results combined with networks extracted from high-resolution topography (e.g., Sonke et al., 2021, this issue) are good candidates to test the efficacy graph theory to produce reasonable estimates of tidal flux asymmetry in estuaries.

A critical gap in understanding what sets the patterns and dynamics in estuarine channel networks is the role of vegetated bank strength, which is a major factor in determining whether a river will be braided or meandering; higher bank strength generally leads to meandering, while cohesionless banks produce more braided rivers (Kleinhans, 2010). At the same time, vegetation on bar surfaces is also a cause of meandering as it reduces or prevents bar cutoff and initiation of braiding (Kleinhans et al., 2018). There are indications in numerical model studies (Braat et al., 2017; Brückner et al., 2020), experiments (Braat et al., 2019) and geological studies (de Haas et al., 2018) that similar mechanisms act in estuaries. This work addresses the connectivity of estuarine channel networks, but future work may benefit from coupling information about the density, type, and spatial extent of cohesive bank and bar surface material and vegetation cover to channel network analyses. Doing so should highlight expected controls of bank strength and bar surface resistance against erosion on channel network patterns along the fluvial–tidal transition.

6 | CONCLUSIONS

This study investigated the structural and dynamical connectivity in estuarine channel networks. Schematics networks were created and analyzed to form a benchmark on which to interpret results from real-world estuarine and delta networks extracted from satellite imagery. The schematic estuaries used were a binary tree (representing a bifurcating delta), symmetric and antisymmetric meshes (representing the mutually evasive flood and ebb channels of estuaries), and a stick network (representing tidal network structure). Thirteen real-world networks were extracted from satellite imagery and were selected to represent a range of estuary network structure types, from nearly tidal networks to bifurcating delta-like systems. Both sets of networks were analyzed using spectral graph theory metrics developed by Tejedor et al. (2015b) for use in deltaic environments in both the flood and ebb directions. The real-world networks were then subsequently compared to the schematic networks. This paper represents the first attempt to use spectral graph theory to analyze estuarine channel network structure and dynamics in both flood and ebb directions, and thus furthers our ability to quantify channel networks in multidirectional environments.

Structural connectivity in estuaries is correlated with network size. As networks get larger, measures of structural connectivity tend to indicate the increased presence of looping structures within the network, resulting in increasing values of link sharing index and number of alternative paths, and a decreasing resistance distance. Analyzing the results within the structural connectivity parameter space indicates that the networks study carries structural characteristics of the mutually evasive flood and ebb channel patterns that typify alluvial estuaries in addition to branching patterns typical of both deltas and tidal networks. However, it is not possible to distinguish between delta-like branching and tidal structures using the structural connectivity metrics presented in this study.

Direction impacts the dynamical connectivity of estuarine networks. Results indicate that networks analyzed in the flood direction exhibit higher values of flux sharing index than in the ebb direction, although no such disparity is apparent for the leakage index. Most of the estuaries networks studied contain many structural connections, resulting in broad flux distributions throughout subnetworks. Flows in the flood direction appear to have a more broadly distributed flux among subnetworks compared to flows in the ebb direction. While many networks appear tree-like, both visually and in terms of structural network indices, dynamical network metrics reveal a tidally caused asymmetry that is mechanistically similar to fluxes in mutually evasive flood- and ebb-dominated channels. The results suggest that systems with significant tidal flows may exhibit estuarine behavior that is not readily apparent from their channel network structure.

ACKNOWLEDGMENTS

We thank the Editor Stuart Lane, one anonymous reviewer, and Alejandro Tejedor for providing valuable comments that helped improve an earlier version of this manuscript. This research was supported by the H2020 European Research Council (grant ERC-CoG 647570 awarded to M.G.K.) and by the Dutch Technology Foundation TTW (grant Vici 016.140.316/13710 to M.G.K.), which is part of the Dutch Research Council (NWO).

CONFLICT OF INTEREST

The authors identify no conflicts of interest.

DATA AVAILABILITY STATEMENT

The data used in this paper are publicly available. The satellite imagery used in this study is available from https://earthexplorer.usgs.gov/ and RivaMap is available at https://github.com/isikdogan/rivamap. Python and Matlab scripts for the network creation and spectral graph theory analysis, respectively, are available at https://github.com/mhiatt262/EstuarineNetworks. Satellite image details are included in Table 2, so that readers can download the same scenes from LANDSAT repositories.

ORCID

Matthew Hiatt https://orcid.org/0000-0003-3680-2542
Elisabeth A. Addink https://orcid.org/0000-0002-0919-6498
Maarten G. Kleinhans https://orcid.org/0000-0002-9484-1673

REFERENCES

Abe, S. & Suzuki, N. (2004) Scale-free network of earthquakes. *EPL (Europhysics Letters)*, 65(4), 581. Available from: https://doi.org/10.1209/epl/i2003-10108-1

Albert, R. & Barabási, A.-L. (2002) Statistical mechanics of complex networks. *Reviews of Modern Physics*, 74, 47–97. Available from: https://doi.org/10.1103/RevModPhys.74.47

Boerema, A. & Meire, P. (2017) Management for estuarine ecosystem services: A review. *Ecological Engineering*, 98, 172–182. Available from: https://doi.org/10.1016/j.ecoleng.2016.10.051

Bolla Pittaluga, M., Repetto, R. & Tubino, M. (2003) Channel bifurcation in braided rivers: Equilibrium configurations and stability. *Journal of Water Resources Research*, 39, 1046. Available from: https://doi.org/10.1029/2001WR001112

Braat, L., van Kessel, T., Leuven, J.R.F.W. & Kleinhans, M.G. (2017) Effects of mud supply on large-scale estuary morphology and development over centuries to millennia. *Earth Surface Dynamics*, 5(4), 617–652. Available from: https://doi.org/10.5194/esurf-5-617-2017

Braat, L., Leuven, J., Lokhorst, I. & Kleinhans, M. (2019) Effects of estuarine mudflat formation on tidal prism and large-scale morphology in experiments. *Earth Surface Processes and Landforms*, 44(2), 417–432. Available from: https://doi.org/10.1002/esp.4504

Bracken, L., Wainwright, J., Ali, G., Tetzlaff, D., Smith, M., Reaney, S. & Roy, A. (2013) Concepts of hydrological connectivity: Research approaches, pathways and future agendas. *Earth-Science Reviews*, 119, 17–34. Available from: https://doi.org/10.1016/j.earscirev.2013.02.001

Brown, J. & Davies, A. (2010) Flood/ebb tidal asymmetry in a shallow sandy estuary and the impact on net sand transport. *Geomorphology*, 114(3), 431–439. Available from: https://doi.org/10.1016/j.geomorph.2009.08.006

Brückner, M.Z.M., Braat, L., Schwarz, C. & Kleinhans, M.G. (2020) What came first, mud or biostabilizers? Elucidating interacting effects in a coupled model of mud, salt marsh, microphytobenthos, and estuarine morphology. *Water Resources Research*, 56(9), e2019WR026945. Available from: https://doi.org/10.1029/2019WR026945

Carrara, F., Altermatt, F., Rodriguez-Iturbe, I. & Rinaldo, A. (2012) Dendritic connectivity controls biodiversity patterns in experimental metacommunities. *Proceedings of the National Academy of Sciences*, 109(15), 5761–5766. Available from: https://doi.org/10.1073/pnas.1119651109

Christensen, A., Twilley, R.R., Willson, C.S. & Castañeda-Moya, E. (2020) Simulating hydrological connectivity and water age within a coastal deltaic floodplain of the Mississippi River Delta. *Estuarine, Coastal and Shelf Science*, 245, 106,995. Available from: https://doi.org/10.1016/j.ecss.2020.106995

Czuba, J.A. & Foufoula-Georgiou, E. (2014) A network-based framework for identifying potential synchronizations and amplifications of sediment delivery in river basins. *Water Resources Research*, 50(5), 3826–3851. Available from: https://doi.org/10.1002/2013WR014227

Czuba, J.A. & Foufoula-Georgiou, E. (2015) Dynamic connectivity in a fluvial network for identifying hotspots of geomorphic change. *Water Resources Research*, 51(3), 1401–1421. Available from: https://doi.org/10.1002/2014WR016139

Dale, M. & Fortin, M.-J. (2010) From graphs to spatial graphs. *Annual Review of Ecology, Evolution, and Systematics*, 41(1), 21–38. Available from: https://doi.org/10.1146/annurev-ecolsys-102209-144718

Dalrymple, R.W. & Choi, K. (2007) Morphologic and facies trends through the fluvial–marine transition in tide-dominated depositional systems: A schematic framework for environmental and sequence-stratigraphic interpretation. *Earth-Science Reviews*, 81(3), 135–174. Available from: https://doi.org/10.1016/j.earscirev.2006.10.002

de Haas, T., Pierik, H., van der Spek, A., Cohen, K., van Maanen, B. & Kleinhans, M. (2018) Long-term evolution of tidal systems: Effects of rivers, coastal boundary conditions, eco-engineering species, inherited relief and human interference. *Earth-Science Reviews*, 177, 139–163. Available from: https://doi.org/10.1016/j.earscirev.2017.10.006

Dronkers, J. (1986) Tidal asymmetry and estuarine morphology. *Netherlands Journal of Sea Research*, 20(2), 117–131. Available from: https://doi.org/10.1016/0077-7579(86)90036-0

Edmonds, D., Paola, C., Hoyal, D. & Sheets, B. (2011) Quantitative metrics that describe river deltas and their channel networks. *Journal of Geophysical Research: Earth Surface*, 116, F04022. Available from: https://doi.org/10.1029/2010JF001955

Fagherazzi, S., Bortoluzzi, A., Dietrich, W.E., Adami, A., Lanzoni, S., Marani, M. & Rinaldo, A. (1999) Tidal networks: 1. Automatic network extraction and preliminary scaling features from digital terrain maps. *Water Resources Research*, 35(12), 3891–3904. Available from: https://doi.org/10.1029/1999WR900236

Friedrichs, C.T. & Aubrey, D.G. (1988) Non-linear tidal distortion in shallow well-mixed estuaries: A synthesis. *Estuarine, Coastal and Shelf Science*, 27(5), 521–545. Available from: https://doi.org/10.1016/0272-7714(88)90082-0

Fryirs, K. (2013) (Dis)connectivity in catchment sediment cascades: A fresh look at the sediment delivery problem. *Earth Surface Processes and Landforms*, 38(1), 30–46. Available from: https://doi.org/10.1002/esp.3242

Heckmann, T. & Schwanghart, W. (2013) Geomorphic coupling and sediment connectivity in an alpine catchment: Exploring sediment cascades using graph theory. *Geomorphology*, 182, 89–103. Available from: https://doi.org/10.1016/j.geomorph.2012.10.033

Heckmann, T., Schwanghart, W. & Phillips, J.D. (2015) Graph theory: Recent developments of its application in geomorphology. *Geomorphology*, 243, 130–146. Available from: https://doi.org/10.1016/j.geomorph.2014.12.024

Hiatt, M., Castañeda-Moya, E., Twilley, R., Hodges, B.R. & Passalacqua, P. (2018) Channel–island connectivity affects water exposure time distributions in a coastal river delta. *Water Resources Research*, 54, 2212–2232. Available from: https://doi.org/10.1002/2017WR021289

Hiatt, M., Sonke, W., Addink, E.A., van Dijk, W.M., van Kreveld, M., Ophelders, T. *et al.* (2020) Geometry and topology of estuary and braided river channel networks automatically extracted from topographic data. *Journal of Geophysical Research: Earth Surface*, 125(1), e2019JF005206. Available from: https://doi.org/10.1029/2019JF005206

Hoitink, A.J.F., Hoekstra, P. & van Maren, D.S. (2003) Flow asymmetry associated with astronomical tides: Implications for the residual transport of sediment. *Journal of Geophysical Research: Oceans*, 108(C10), 3315. Available from: https://doi.org/10.1029/2002JC001539

Horton, R.E. (1945) Erosional development of streams and their drainage basins: Hydrophysical approach to quantitative morphology. *GSA Bulletin*, 56(3), 275–370. Available from: https://journals.sagepub.com/doi/10.1177/030913339501900406

Isikdogan, F., Bovik, A. & Passalacqua, P. (2015) Automatic channel network extraction from remotely sensed images by singularity analysis. *IEEE Geoscience and Remote Sensing Letters*, 12(11), 2218–2221. Available from: https://doi.org/10.1109/LGRS.2015.2458898

Isikdogan, F., Bovik, A. & Passalacqua, P. (2017) *RivaMap: An automated river analysis and mapping engine*, Vol. 202, pp. 88–97. Available from: https://doi.org/10.1016/j.rse.2017.03.044

Jencso, K.G., McGlynn, B.L., Gooseff, M.N., Wondzell, S.M., Bencala, K.E. & Marshall, L.A. (2009) Hydrologic connectivity between landscapes and streams: Transferring reach- and plot-scale understanding to the catchment scale. *Water Resources Research*, 45(4), w04428. Available from: https://doi.org/10.1029/2008WR007225

Jeuken, M.C.J.L. & Wang, Z.B. (2010) Impact of dredging and dumping on the stability of ebb–flood channel systems. *Coastal Engineering*, 57, 553–66. Available from: https://doi.org/10.1016/j.coastaleng.2009.12.004

Kang, J. & Jun, K. (2003) Flood and ebb dominance in estuaries in Korea. *Estuarine, Coastal and Shelf Science*, 56(1), 187–196. Available from: https://doi.org/10.1016/S0272-7714(02)00156-7

Kennish, M.J. (2002) Environmental threats and environmental future of estuaries. *Environmental Conservation*, 29(1), 78–107. Available from: https://doi.org/10.1017/S0376892902000061

Kleinhans, M.G. (2010) Sorting out river channel patterns. *Progress in Physical Geography*, 34(3), 287–326. Available from: https://doi.org/10.1177/0309133310365300

Kleinhans, M.G., Ferguson, R.I., Lane, S.N. & Hardy, R.J. (2013) Splitting rivers at their seams: Bifurcations and avulsion. *Earth Surface Processes and Landforms*, 38(1), 47–61. Available from: https://doi.org/10.1002/esp.3268

Kleinhans, M., de Vries, B., Braat, L. & van Oorschot, M. (2018) Living landscapes: Muddy and vegetated floodplain effects on fluvial pattern in

an incised river. *Earth Surface Processes and Landforms*, 43, 1618–1632. Available from: https://doi.org/10.1002/esp.4437

Lanzoni, S. & Seminara, G. (2002) Long-term evolution and morphodynamic equilibrium of tidal channels. *Journal of Geophysical Research: Oceans*, 107(C1), 1–1–1-13. Available from: https://doi.org/10.1029/2000JC000468

Leuven, J., Kleinhans, M., Weisscher, S. & van der Vegt, M. (2016) Tidal sand bar dimensions and shapes in estuaries. *Earth-Science Reviews*, 161, 204–223. Available from: https://doi.org/10.1016/j.earscirev.2016.08.004

Leuven, J., Haas, T., Braat, L. & Kleinhans, M. (2017) *Topographic forcing of tidal sand bar patterns for irregular estuary planforms*, Vol. 43, pp. 172–186. Available from: https://doi.org/10.1002/esp.4166

Leuven, J.R.F.W., Braat, L., van Dijk, W.M., de Haas, T., van Onselen, E.P., Ruessink, B.G. & Kleinhans, M.G. (2018) Growing forced bars determine nonideal estuary planform. *Journal of Geophysical Research: Earth Surface*, 123(11), 2971–2992. Available from: https://doi.org/10.1029/2018JF004718

Marra, W.A., Kleinhans, M.G. & Addink, E.A. (2014) Network concepts to describe channel importance and change in multichannel systems: Test results for the Jamuna River, Bangladesh. *Earth Surface Processes and Landforms*, 39(6), 766–778. Available from: https://doi.org/10.1002/esp.3482

Muralidhar, G.S., Bovik, A.C. & Markey, M.K. (2012) A new singularity index. In *2012 19th IEEE International Conference on Image Processing*, Orlando, FL, pp. 1873–1876.

Newman, M.E.J. (2003) The structure and function of complex networks. *SIAM Review*, 45(2), 167–256. Available from: https://doi.org/10.1137/S003614450342480

Newman, M. (2010) *Networks: An introduction*. Oxford: Oxford University Press.

Olliver, E.A., Edmonds, D.A. & Shaw, J.B. (2020) Influence of floods, tides, and vegetation on sediment retention in Wax Lake Delta, Louisiana, USA. *Journal of Geophysical Research: Earth Surface*, 125(1), e2019JF005316. Available from: https://doi.org/10.1029/2019JF005316

Passalacqua, P. (2017) The Delta Connectome: A network-based framework for studying connectivity in river deltas. *Geomorphology*, 277, 50–62. Available from: https://doi.org/10.1016/j.geomorph.2016.04.001, connectivity in Geomorphology from Binghamton 2016.

Phillips, J.D., Schwanghart, W. & Heckmann, T. (2015) Graph theory in the geosciences. *Earth-Science Reviews*, 143, 147–160. Available from: https://doi.org/10.1016/j.earscirev.2015.02.002

Prandle, D. (2003) Relationships between tidal dynamics and bathymetry in strongly convergent estuaries. *Journal of Physical Oceanography*, 33(12), 2738–2750.

Prandle, D. (2004) How tides and river flows determine estuarine bathymetries. *Progress in Oceanography*, 61(1), 1–26. Available from: https://doi.org/10.1016/j.pocean.2004.03.001

Pringle, C. (2003) What is hydrologic connectivity and why is it ecologically important? *Hydrological Processes*, 17(13), 2685–2689. Available from: https://doi.org/10.1002/hyp.5145

Rinaldo, A., Fagherazzi, S., Lanzoni, S., Marani, M. & Dietrich, W.E. (1999a) Tidal networks: 2. Watershed delineation and comparative network morphology. *Water Resources Research*, 35(12), 3905–3917. Available from: https://doi.org/10.1029/1999WR900237

Rinaldo, A., Fagherazzi, S., Lanzoni, S., Marani, M. & Dietrich, W.E. (1999b) Tidal networks: 3. Landscape-forming discharges and studies in empirical geomorphic relationships. *Water Resources Research*, 35(12), 3919–3929. Available from: https://doi.org/10.1029/1999WR900238

Robinson, A.H.W. (1960) Ebb–flood channel systems in sandy bays and estuaries. *Geography*, 45(3), 183–199. Available from: https://www.jstor.org/stable/40565158

Rodriguez-Iturbe, I. & Rinaldo, A. (1997) *Fractal river basins: Chance and self-organization*. (1st ed.). New York, NY: Cambridge University Press.

Ruddell, B. & Kumar, P. (2009a) Ecohydrologic process networks: 1. Identification. *Water Resources Research*, 45, W03419. Available from: https://doi.org/10.1029/2008WR007279

Ruddell, B. & Kumar, P. (2009b) Ecohydrologic process networks: 2. Analysis and characterization. *Water Resources Research*, 45, W03420. Available from: https://doi.org/10.1029/2008WR007280

Savenije, H.H.G. (2015) Prediction in ungauged estuaries: An integrated theory. *Water Resources Research*, 51(4), 2464–2476. Available from: https://doi.org/10.1002/2015WR016936

Sendrowski, A. & Passalacqua, P. (2017) Process connectivity in a naturally prograding river delta. *Water Resources Research*, 53(3), 1841–1863. Available from: https://doi.org/10.1002/2016WR019768

Shreve, R.L. (1966) Statistical law of stream numbers. *The Journal of Geology*, 74(1), 17–37. Available from: https://doi.org/10.1086/627137

Smart, J. & Moruzzi, V. (1972) Quantitative properties of delta channel networks. *Zeitschrift für Geomorphologie*, 16(3), 283–300.

Sonke, W., Kleinhans, M.G., Speckmann, B., van Dijk, W.M., Hiatt, M. & (2021) Alluvial connectivity in multi-channel networks in rivers and estuaries. *Earth Surface Processes and Landforms*. Available from: https://doi.org/10.1002/esp.5261

Stieglitz, M., Shaman, J., McNamara, J., Engel, V., Shanley, J. & Kling, G.W. (2003) An approach to understanding hydrologic connectivity on the hillslope and the implications for nutrient transport. *Global Biogeochemical Cycles*, 17(4), 1105. Available from: https://doi.org/10.1029/2003GB002041

Strahler, A.N. (1957) Quantitative analysis of watershed geomorphology. *Eos: Transactions of the American Geophysical Union*, 38(6), 913–920. Available from: https://doi.org/10.1029/TR038i006p00913

Tejedor, A., Longjas, A., Zaliapin, I. & Foufoula-Georgiou, E. (2015a) Delta channel networks: 1. A graph-theoretic approach for studying connectivity and steady state transport on deltaic surfaces. *Water Resources Research*, 51(6), 3998–4018. Available from: https://doi.org/10.1002/2014WR016577

Tejedor, A., Longjas, A., Zaliapin, I. & Foufoula-Georgiou, E. (2015b) Delta channel networks: 2. Metrics of topologic and dynamic complexity for delta comparison, physical inference, and vulnerability assessment. *Water Resources Research*, 51(6), 4019–4045. Available from: https://doi.org/10.1002/2014WR016604

Tejedor, A., Longjas, A., Caldwell, R., Edmonds, D.A., Zaliapin, I. & Foufoula-Georgiou, E. (2016) Quantifying the signature of sediment composition on the topologic and dynamic complexity of river delta channel networks and inferences toward delta classification. *Geophysical Research Letters*, 43(7), 3280–3287. Available from: https://doi.org/10.1002/2016GL068210

Tetzlaff, D., Soulsby, C., Bacon, P.J., Youngson, A.F., Gibbins, C. & Malcolm, I.A. (2007) Connectivity between landscapes and riverscapes: A unifying theme in integrating hydrology and ecology in catchment science? *Hydrological Processes*, 21(10), 1385–1389. Available from: https://doi.org/10.1002/hyp.6701

Townend, I. (2012) The estimation of estuary dimensions using a simplified form model and the exogenous controls. *Earth Surface Processes and Landforms*, 37(15), 1573–1583. Available from: https://doi.org/10.1002/esp.3256

Van der Wegen, M. & Roelvink, J. (2012) Reproduction of estuarine bathymetry by means of a process-based model: Western Scheldt case study, the Netherlands. *Geomorphology*, 179, 152–167. Available from: https://doi.org/10.1016/j.geomorph.2012.08.007

van Dijk, W.M., Hiatt, M.R., van der Werf, J.J. & Kleinhans, M.G. (2019) Effects of shoal margin collapses on the morphodynamics of a sandy estuary. *Journal of Geophysical Research: Earth Surface*, 124(1), 195–215. Available from: https://doi.org/10.1029/2018JF004763

van Veen, J. (1950) Eb- en vloedschaar systemen in de Nederlandse getijwateren. *Journal of the Royal Dutch Geographical Society*, 67, 303–325. in Dutch.

Wainwright, J., Turnbull, L., Ibrahim, T.G., Lexartza-Artza, I., Thornton, S. F. & Brazier, R.E. (2011) Linking environmental regimes, space and time: Interpretations of structural and functional connectivity. *Geomorphology*, 126(3–4), 387–404. Available from: https://doi.org/10.1016/j.geomorph.2010.07.027

Wang, Z., De Vries, M., Fokkink, R. & Langerak, A. (1995) Stability of river bifurcations in ID morphodynamic models. *Journal of Hydraulic research*, 33(6), 739–750.

Wang, Z., Jeuken, M., Gerritsen, H., de Vriend, H. & Kornman, B. (2002) Morphology and asymmetry of the vertical tide in the Westerschelde estuary. *Continental Shelf Research*, 22(17), 2599–2609. Available from: https://doi.org/10.1016/S0278-4343(02)00134-6

Watts, D.J. (2004) The "new" science of networks. *Annual Review of Sociology*, 30(1), 243–270. Available from: https://doi.org/10.1146/annurev.soc.30.020404.104342

Wohl, E., Magilligan, F.J. & Rathburn, S.L. (2017) Introduction to the special issue: Connectivity in geomorphology. *Geomorphology*, 277, 2016. Available from: https://doi.org/10.1016/j.geomorph.2016.11.005, connectivity in Geomorphology from Binghamton.

Xu, H. (2006) Modification of normalised difference water index (NDWI) to enhance open water features in remotely sensed imagery. *International Journal of Remote Sensing*, 27(14), 3025–3033. Available from: https://doi.org/10.1080/01431160600589179

Zaliapin, I., Foufoula-Georgiou, E. & Ghil, M. (2010) Transport on river networks: A dynamic tree approach. *Journal of Geophysical Research: Earth Surface*, 115(F2), f00A15. Available from: https://doi.org/10.1029/2009JF001281

Zolezzi, G., Bertoldi, W. & Tubino, M. (2006) Morphological analysis and prediction of river bifurcations, *Braided rivers: Process, deposits, ecology and management. Special Publication Number 36 of the International Association of Sedimentologists*. Oxford: Blackwell, pp. 233–256. Available from: https://doi.org/10.1002/9781444304374.ch11

SUPPORTING INFORMATION

Additional supporting information may be found in the online version of the article at the publisher's website.

How to cite this article: Hiatt, M., Addink, E.A. & Kleinhans, M.G. (2022) Connectivity and directionality in estuarine channel networks. *Earth Surface Processes and Landforms*, 47(3), 807–824. Available from: https://doi.org/10.1002/esp.5286